Confinement Effects on the Structure of Entropy-Induced Supercrystals

Claire Goldmann, Wajdi Chaâbani, Claire Hotton, Marianne Impéror-Clerc, Adrien Moncomble, Doru Constantin, Damien Alloyeau, Cyrille Hamon

Confinement effects on the structure of entropy-induced supercrystals

Claire Goldmann,[1] Wajdi Chaâbani,[1] Claire Hotton,[1] Marianne Impéror-Clerc,[1] Adrien Moncomble,[2] Doru Constantin, [3]* Damien Alloyeau,[2]* Cyrille Hamon[1]*

[1] Université Paris-Saclay, CNRS, Laboratoire de Physique des Solides, 91405 Orsay, France.

[2] Université Paris-Cité, CNRS, Laboratoire Matériaux et Phénomènes Quantiques, 75013 Paris, France.

[3] Institut Charles Sadron, CNRS and Université de Strasbourg, 67034 Strasbourg, France.

KEYWORDS: Plasmonic nanoparticles, depletion-induced self-assembly, Liquid cell TEM, self-assembly in confinement, disassembly under electron irradiation, Small Angle X-Ray Scattering.

E-mail: constantin@unistra.fr, damien.alloyeau@u-paris.fr, cyrille.hamon@universite-paris-saclay.fr

Abstract

Depletion-induced self-assembly is routinely used to separate plasmonic nanoparticles (NPs) of different shapes, but less often for its ability to create supercrystals (SCs) in suspension. Therefore, these plasmonic assemblies have not yet reached a high level of maturity and their in-depth characterization by a combination of in situ techniques is still very much needed. In this work, we assembled gold triangles (AuNTs) and silver nanorods (AgNRs) by depletion-induced self-assembly. Small Angle X-ray Scattering (SAXS) and scanning electron microscopy (SEM) analysis shows that the AuNTs and AgNRs form 3D and 2D hexagonal lattices in bulk respectively. The colloidal crystals were also imaged by in situ Liquid-Cell Transmission Electron Microscopy. Under confinement, the affinity of the NPs for the liquid cell windows reduces their ability to stack perpendicularly to the membrane and lead to SCs with a lower dimensionality than their bulk counterparts. Moreover, extended beam irradiation leads to disassembly of the lattices, which is well described by a model accounting for the desorption kinetics highlighting the key role of the NP-membrane interaction in the structural properties of SCs in the liquid-cell. Our results shed light on the reconfigurability of NP superlattices obtained by depletion-induced self-assembly, which can rearrange under confinement.

Introduction

Silver and gold nanoparticles (NPs) have garnered sustained interest over the past 25 years because of their exceptional interaction with light, originating from localized surface plasmon resonances. Novel materials made by colloidal design can be used to control the flow of light through interparticle plasmonic coupling.[1] One outstanding challenge is to endow these assemblies with a structural response under specific external stimuli,[2] which can actuate a broad range of nanoscale forces.[3] Among these, depletion forces can be used to induce the self-assembly of NPs in a reversible manner.[4] In particular, surfactant micelles induce NP flocculation by depletion-induced attraction. Since this process leads to an overall increase of the entropy of the system by excluded volume interaction, it is alternatively denoted as entropy-driven self-assembly.[5] The amplitude of the attraction is proportional to the concentration and radius of the surfactant micelles and to the contact area between two particles. By this process, NPs featuring a high contact area form superstructures that sediment to the bottom of the flask, while the smaller (or rounder) NPs remain in suspension. The process is reversible: the NPs assemble and then redisperse upon dilution. Depletion-induced self-assembly has been used to

separate plasmonic NPs of different shapes,[6] or supercrystals (SCs)[7] (when combined with controlled evaporation) but very little for its ability to shape SCs.[8] For instance, Young et al. have shown by small angle X-ray scattering (SAXS) that depletion forces could be tuned in situ by changing the surfactant concentration, the temperature and the ionic strength of the solution, which in turn modify superlattice parameters.[8a] Elsewhere, Yang et al. studied the nucleation and growth of the SCs by in situ SAXS and showed the formation of micron-sized SCs, which packed together during sedimentation to form highly oriented structures.[8c]

Liquid-Cell Transmission Electron Microscopy (LCTEM) is an emerging technique for studying the dynamic of individual soft, hard or hybrid nanomaterials in a liquid of controlled composition and temperature.[9] In particular, it has led to breakthroughs in NP synthesis and self-assembly.[9c, 10] Notably, the effects of NP shape, NP-substrate interactions and the structure and charge of the ligand shell on the structure and dynamics of the SCs has been investigated and optimized to better understand the nanoscale forces driving SC formation and to visualize the crystallization processes of large 3D nanocrystal superlattices by LCTEM.[11] Nevertheless, LCTEM observations are not always directly comparable to bulk experiments because of the presence of interfaces, limited mass transport and radiolysis effects. Indeed, NPs are imaged near a surface with a charge state that depends on the illumination conditions and in a confined environment a few hundred nanometer thick, which slows down their diffusion.[12] Another challenge of this technique is understanding the effects of radiolysis on the solution chemistry and soft-material damage.[13] Thus, revealing the differences between bench-scale synthesis and in situ TEM data is essential to better use LCTEM results in nanomaterial and SC fabrication. A way of meeting this challenge is to perform complementary in situ characterization such as SAXS, spectroscopy or, alternatively, computer simulations.[10b, 10c, 14]

In this work, we synthesized and assembled gold triangles (AuNTs) and silver nanorods (AgNRs) by depletion-induced self-assembly. We analyzed the structure of the SCs with a multi-scale approach from the bulk solution (SAXS and ex situ scanning electron microscopy (SEM)) to the single NP level (in situ LCTEM). Thus, we revealed how the confinement within the liquid-cell affects the structural properties of SCs and we quantitatively studied their evolution under electron irradiation to evaluate the possible driving forces of these structural reconfigurations.

Results and discussion

Triangular nanoprisms (AuNTs, 75 nm ± 4 nm in edge length and 30 nm ± 5 nm in thickness) and silver nanorods (AgNRs, 216 ± 19.6 nm in length and 27 ± 1.7 nm in width) were prepared by seed-mediated growth from mono-twinned gold seeds and penta-twinned gold bipyramids, respectively (**Figure 1 a, e and Figure S1 and S2**).[15]

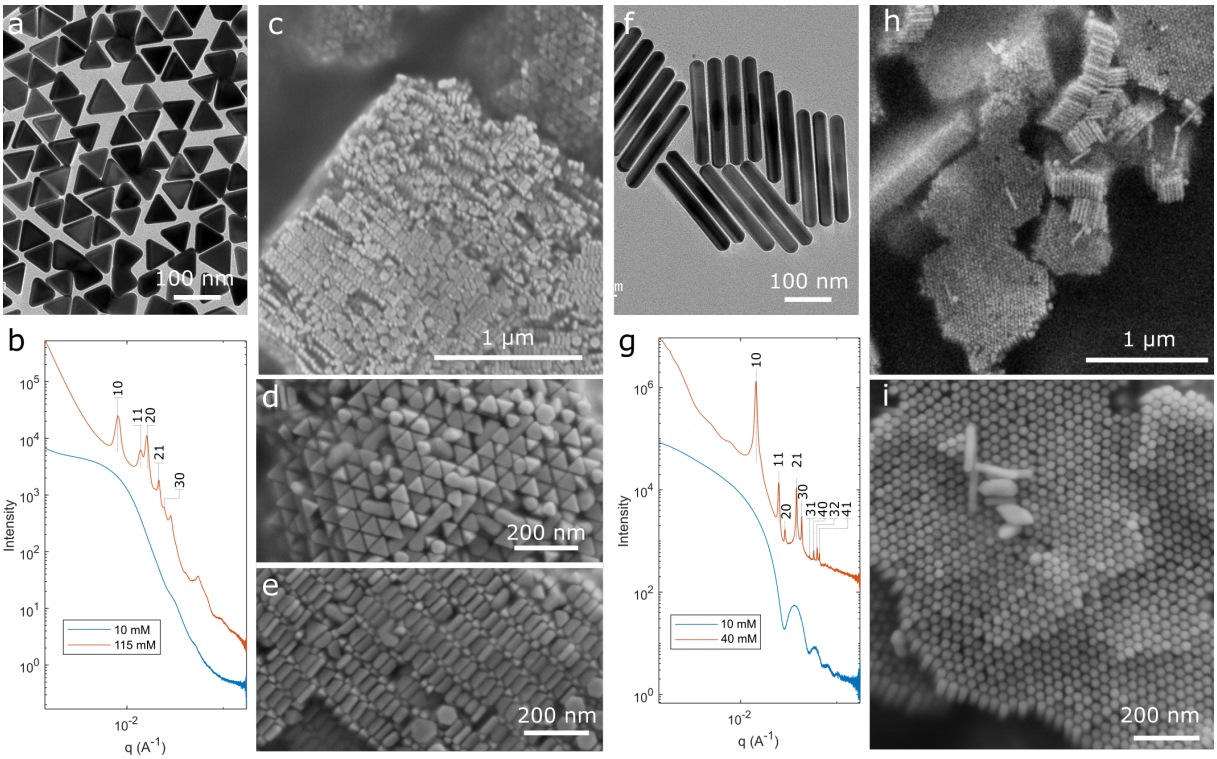

Figure 1: Depletion-induced self-assembly of AuNTs and AgNRs. a) TEM image of AuNTs, b) SAXS data with curves corresponding to two AuNT suspensions loaded with 10 mM CTAC (blue) and 115 mM CTAC (orange). c-e) SEM images of AuNTs assemblies at different magnification. f) TEM image of the AgNRs. g) SAXS data with curves corresponding to two AgNRs suspension loaded with 10 mM CTAC (blue) and 40 mM CTAC (orange). h-i) SEM images of AgNR assemblies at different magnification.

The synthesis of AuNTs and AgNRs was performed using cetyltrimethylammonium chloride (CTAC) as colloidal stabilizer and shape directing agent. CTAC was also used as osmotic agent in depletion-induced self-assembly experiments. The suspensions were probed by SAXS (**Figure 1 b, f**). Colloidal crystallization is observed above a certain threshold CTAC concentration, which varies with the shape of the NPs (115 mM for the AuNTs and 40 mM for the AgNRs). At 10 mM CTAC, the SAXS curve corresponds to the form factor (in blue) of the NPs, indicating well-dispersed suspensions. At higher CTAC concentration, Bragg peaks indicate not only the flocculation but also the crystallization of SCs. For both AuNTs and AgNRs the spectra exhibit Bragg peaks in 1:√3:2:√7:3 progression, characteristic of the in-

plane hexagonal arrangement of the NPs. In the case of the AuNTs, the unit cell is composed of two parallel NPs having opposite orientation (rotated by 60°) and shifted along their normal from one layer to another, defining an interlocked hexagonal structure. This organization was confirmed on ex situ scanning electron microscopy (SEM) images (**Figure 1c-d and Figure S3**). This particular configuration stems from the arrangement between the basal facets and the lateral facets of the beveled AuNTs.[7e] In the case of the AgNRs no lamellar organization is detected, indicating that in solution the nanorods form monolayers without interlayer stacking. Confirming this analysis, isolated nanorod rafts were observed on ex situ SEM images, with some lamellar organization that can be ascribed to additional ordering by evaporation-induced self-assembly (**Figure 1g-h** and **Figure S3**).[16] These two SC structures schematized in **Figure 2** show that shape anisotropy can be used to form superstructure with controlled dimensionality by favoring side-to-side over end-to-end packing.

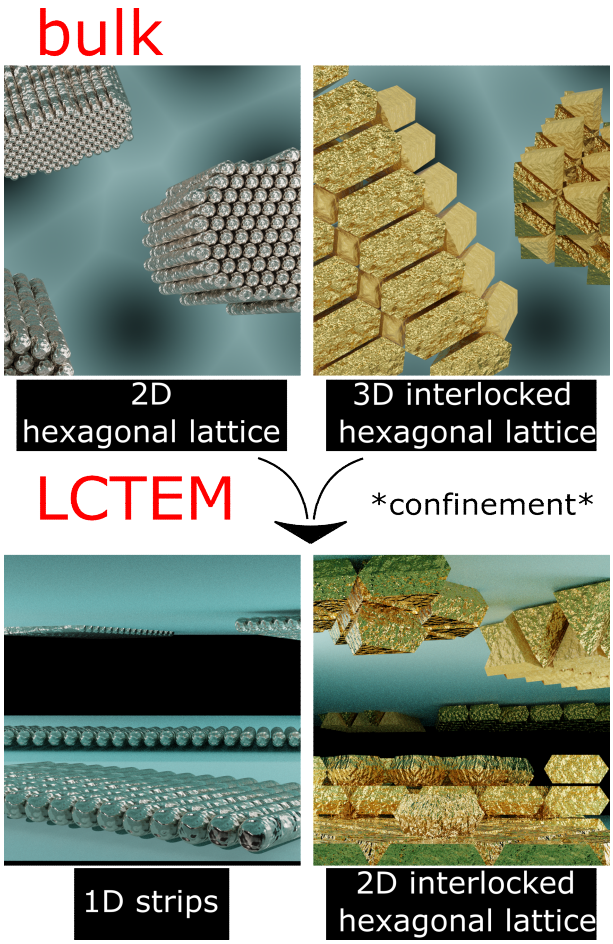

Figure 2: Schemes depicting the superlattices obtained by depletion-induced self-assembly in bulk and after loading in the LCTEM chip.

We then studied the colloidal crystals in LCTEM in the presence of 115 mM CTAC for the AuNTs and 40 mM CTAC for the AgNRs. The suspension containing assembled AuNTs and

AgNRs were separately confined between two SiN membranes with 500 nm spacing layer. At first, a remarkable re-ordering of the NPs is observed in the liquid cell. Indeed, the AgNRs form supramolecular wires (hereafter denoted as strips) with an average size of 2.9 ±1.9 µm in which nanorods are stacked side by side (**Figure 3a-b**). These strips also tend to stack side by side along the SiN membrane with 5 ± 3 units per stack, but no 3D stacking was observed. SCs made of AuNTs are observed along horizontal or vertical orientations with respect to the membranes. The in-plane hexagonal arrangement is observed when the AuNTs lay flat on the SiN membrane and the interlocked stacking is seen when the AuNTs stand perpendicularly to the SiN membrane (**Figure 3c-d**). Contrast analysis of the in-plane hexagonal arrangements shows that the face-to-face stacking of the NPs in the direction perpendicular to the membrane is limited to between 2 and 3 NPs and these SCs in horizontal orientation are mainly composed of NP monolayers and bilayers (**Figure S4**). However, up to ten layers of AuNTs are directly observed when the face to face stacking goes along the membrane plane (i.e. for AuNTs in vertical orientation) but crystallization perpendicular to the substrate is also very limited (**Figure 3d**). Those type of low dimensionality structures were always observed by LCTEM. The reconfiguration of the lattice therefore occurs during the sealing process and occurs within less than 15 minutes that is the delay time between the preparation of the chip and the observation of the samples by LCTEM.

In the following, we compare the size and structure of SCs confined in the liquid-cell and in bulk solution. The median surface area of AgNRs in beakers was measured by ex-situ optical microscopy to be 0.35 μm^2 with first quantile (Q1) of 0.15 μm^2 and Q3 = 0.77 μm^2. Similar analysis on the AuNTs revealed a median surface area of 0.32 μm^2 with Q1 = 0.16 μm^2 and Q3 = 0.61 μm^2 (**Figure S5**). This is in reasonable agreement with the extension of the monocrystals measured by in situ SAXS (from the full width at half maximum of the SAXS peaks) to be about 1 to 2 µm for both AuNTs and AgNRs. Furthermore, the edge-to-edge interparticle distances (d_{e-e}) were deduced from SAXS measurements to be 23 nm for the AgNRs while the AuNTs were separated by 13 nm in the hexagonal plane. In LCTEM, the SC's surface area was measured to be 0.7 ± 0.8 μm^2 and 0.6 ± 0.4 μm^2 for the AuNTs and the AgNRs, respectively. Also in good agreement with the SAXS analysis, d_{e-e} was measured by LCTEM to be 21 nm for the AgNRs (**Figure S6**) and 13 nm for the AuNTs in the hexagonal plane (**Figure S7**). These edge-to-edge distances were not affected by the electron dose rate (**Figure S6**). Note that the out of plane stacking distance of AuNTs was measured to be 15 nm by LCTEM when the AuNTs are observed in vertical orientation (**Figure S7**). This out of plane distance could not be

confirmed by SAXS because the expected 001 peak cannot be measured: it presumably overlaps with the 110 and 200 ones and is very weak because of the high relative size dispersion in thickness of the AuNTs (17%). These large interparticle spacings (more than two surfactant bilayers[17]) result from the balance between attractive depletion and repulsive electrostatic interactions.[8a] For comparison, in the dried state, the interparticle distance was found to be always below 5 nm by ex situ MEB analysis (**Figure S8**). Although the SCs size and lattice parameters are of the same order in bulk solution and in the liquid-cell, the volume reduction or the affinity of metal NPs for the SiN membrane favor the formation of 2D SCs with similar structural features of the 3D SCs revealed in bulk experiments (see schematic representations in **Figure 2**).

In complementary experiments, we tried to modify the volume of the liquid cell and the affinity of the NPs for the SiN membrane to evaluate the respective impact of these two parameters. Interestingly, SCs with similar structures are observed in liquid cells with spacers of only 150 nm (**Figure S9**). LCTEM sample preparation typically involves a plasma-cleaning step of the SiN membrane to remove contamination and improve surface wetting. In LCTEM experiments performed with uncleaned liquid-cells, the NPs forms large 3D aggregates that diffuse in the liquid, presumably because of lower affinity of NPs for membranes with reduced hydrophilicity and surface charge (See **Video S1**).[12b] The high mobility of these large assemblies prevents their structural analysis. Nevertheless, these two experiments indicate that the lower dimensionality of SCs observed in liquid cells compared to the SCs formed in beakers is very likely due to membrane interaction rather than reduced volume effects.

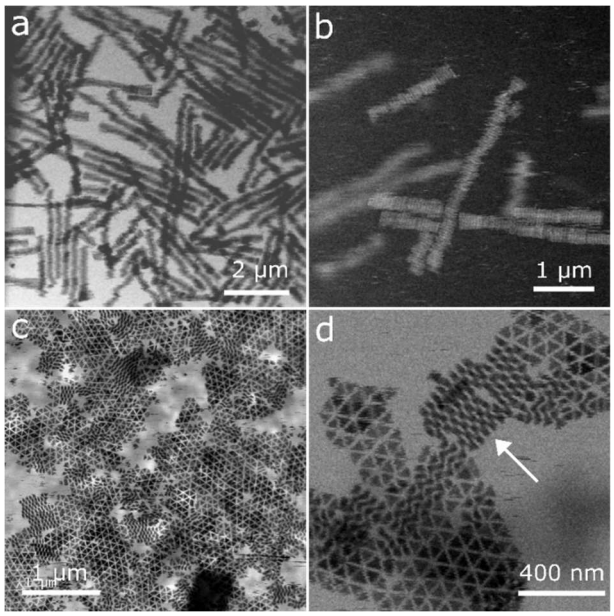

Figure 3: Depletion-induced self-assembly of AuNTs and AgNRs in confinement. a-d) STEM images of (a-b) AgNRs assemblies and (c-d) AuNTs assemblies at different magnifications within liquid-cell. Images are recorded in high-angle annular dark field (b) or bright field (a, c, d) modes. Arrow in (d) point toward a superlattice of standing AuNTs (i.e. in vertical orientation).

Prolonged LCTEM observation led to the disassembly of the nanostructures by progressive NP ejection (**Figure 4, Video S2-S3**). In the case of AgNRs, NP ejection occurred preferentially from the ends of the strips. Some instances of strips breaking into two parts and of strip reformation during the disassembly process were observed (**Figure 4b**). Hence, these assemblies resemble "living polymers," evolving via a step-growth mechanism because both monomers and oligomers can attach to the reactive ends of the strips.[18] In the case of AuNTs, NP ejection occurred preferentially at the edge of the lattice, rather than within the SCs, presumably because more bonds (membrane-NPs and NPs-NPs) would need to be broken in the latter case. Fast desorption / readsorption processes are observed at the edge of the SCs (**Video S3**). When a vacancy appeared within the core of the SCs, the hole rapidly grew within the SC, leading to an increased rate of lattice disassembly. These two experiments were performed at different dose rates: 0.066 e/A^2s for the AgNRs and 0.592 e/A^2s for the AuNTs and the disassembly was faster for the AuNTs (40s) compared to the AgNRs (150s). It is worth noting that the AgNRs strips diffuse in the liquid during TEM observations while the SCs made of AuNTs stay attached to the window, which can be explained by the different affinity of Au and Ag NPs for the SiN membrane (see below). More time-lapse STEM images are shown in the SI (**Figure S10-S13**).

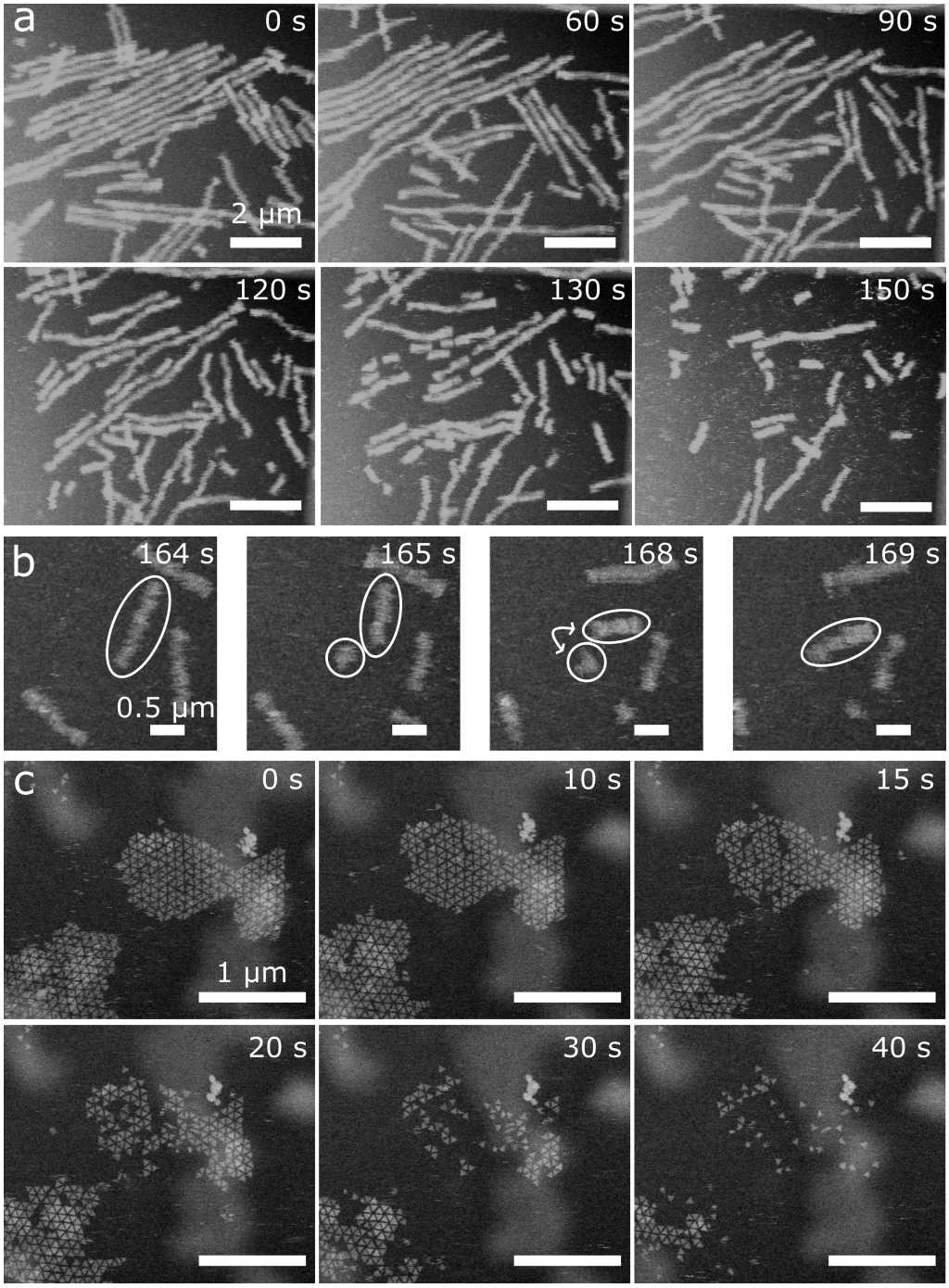

Figure 4. Time-resolved disassembly of plasmonic superlattices by LCTEM. a-c) Time-lapse STEM-HAADF images showing the disassembly of (a-b) AgNR threads and (c) 2D AuNT hexagonal lattices respectively. Outlines in (b) indicate the dissociation of a thread in two parts, which reform as a single thread a few second later. The dose rate was 0.066 e/A^{2}s in (a-b) and 0.592 e/A^{2}s in (c).

We then investigated the disassembly kinetics. Experiments were performed at different dose rate, for both AgNRs (**Figure 5**) and AuNTs (**Figure S16**), and the number of particles N(t) at each time was retrieved via automatic image analysis. We define the time-dependent coverage

n(t) = N(t)/N(0), which is represented against time in **Figure 5**. In all cases, the disassembly kinetics is similar: it starts with a slow decline, followed by a dramatic acceleration (**Figure 5**). In order to describe the experimental situation, we need to account for the interactions that hold the SC together (depletion, van der Waals etc.), denoted below by "cohesion" and for those maintaining the SC in contact with the membrane (electrostatics, depletion, etc.), and generically termed "adhesion". Thus, in our model (see the SI for details), a SC consists of a (time-dependent) number of particles N(t), each one interacting with the substrate and with its neighbors via the adhesion and cohesion energies E_A and E_C, respectively. To preserve the generality of the model, we do not attempt to further separate these essential ingredients into components. Both E_A and E_C are presumably attractive in the absence of the electron beam (because the SC is stable and remains attached to the substrate), but they might become increasingly repulsive under the beam, for instance as the membrane and/or the particles become similarly charged. The desorption rate can be written as $k_D(n) = Aexp[-Bn(t)]$, with $A = Kexp\left[-\frac{E_A}{k_BT}\right]$ and $B = \frac{zE_C}{k_BT}$. K is a (presumably very large) kinetic pre-factor accounting for the desorption rate in the absence of any interaction and z is the coordination number (for instance, z = 4 for a planar square lattice). The fits for the AgNRs are quite good (see **Figure 5**, top), especially since the model only has four free coefficients: A, B, the initial number of particles N(0) and a residual number of fixed particles N(∞). Parameters A and B are shown in **Figure 5** (bottom). We can conclude that B (and thus E_C) remains constant, while A changes with $\dot{d}$, due to a change in either K or E_A. The dependence of A (and hence of k_D) on the dose rate is linear: $A = \alpha\dot{d}$, with α=11±1.5 $Å^2/e^-$.

The same treatment can be applied to SC formed by triangles, with very similar qualitative conclusions but with a much lower constant α=0.8±0.12 $Å^2/e^-$ (**Figure S17**), implying that AuNTs were more difficult to eject. This can be explained by the stronger interaction of the AuNTs with the membrane, most likely due to their higher surface area in contact with the membrane. Note also that the desorption kinetics varied with the two possible arrangements of the AuNTs (vertical or horizontal orientations), which do not disassemble at the same rate. For instance, in the two experiments shown in **Figure S18**, the AuNTs were either all flat or consisted of a mixture of flat AuNTs and standing AuNTs respectively. Although we used the same dose rate (0.592 e/ $Å^2$s), their disassembly kinetics do not overlap (**Figure S16**), since the initial arrangement of the AuNTs was not equivalent. This experiment shows that standing AuNTs are less stable against desorption than lying AuNTs because this configuration minimizes their interaction with the membrane.

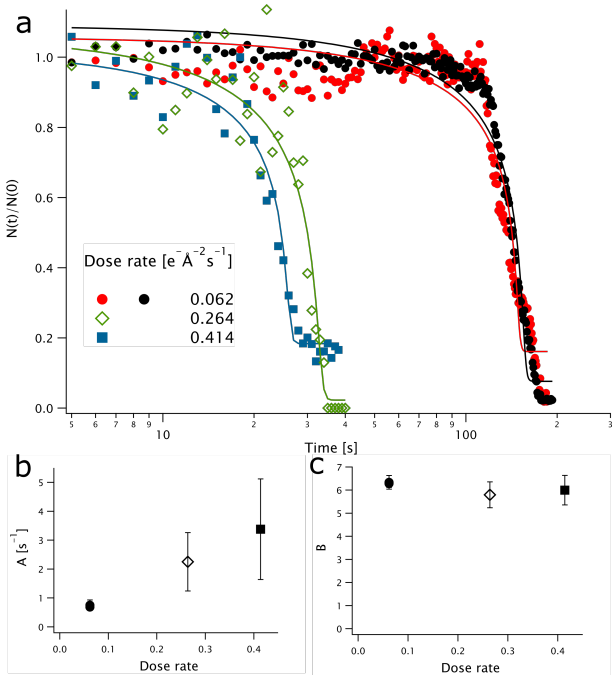

Figure 5: SC survival under electron irradiation. a) Normalized number of particles N(t)/N(0) in AgNR SCs at different dose rates (symbols) and fits with the kinetic model described in the text (lines). b-c) Fit parameters A and B (see text for the definitions).

Next, we discuss the possible mechanisms of NP disassembly under electron beam irradiation. Although we worked in the low dose conditions (< 1 e.Å^{-2}.s^{-1}) that are typically used for imaging organic soft matter,[10c] a beam-induced disassembly process is revealed in all experiments. Electron irradiation is known to affect both the liquid and the insulating SiN membrane, in a dose-rate dependent manner, and to modify (i) the ionic strength, (ii) the pH, (iii) the concentration of reactive oxygen species and iv) the surface charge of the SiN membrane. The production of ionic species by radiolysis would result in a decrease of the distance between the NPs, as reported in other studies,[8a, 10c, 14b] but this was not observed in the present work (**Figure S6**). Moreover, given the quaternary amine functionality of CTAC, assemblies are expected to be robust with regard to pH. The disassembly process could be induced by radiolysis products (mainly hydroxyl radicals), which are known to favor cross-linking or chain scission in organic polymers depending on the dose rate.[19] In the framework of LCTEM experiments, Dissanayake et al.[13c] showed that polymerization of branched polyethylenimine occurs at low cumulative dose, followed by chain scission at higher cumulative dose. Interestingly, this work and others[20] describe metal NPs as hotspots for radiolysis in the liquid-cell. Taken together, a reasonable hypothesis explaining our observations is a disassembly process mediated by the degradation of the CTAC ligands at the

surface of the NPs by polymerization and/or chain scission. The latter mechanism would result in the production of insoluble alkane and tertiary amine (through cleavage of quaternary ammonium) and/or a mixture of short amphiphilic ligands and insoluble alkane (through cleavage of quaternary ammonium) and/or a mixture of short amphiphilic ligands and insoluble alkane (through cleavage of the aliphatic chain). This would in turn induce the colloidal destabilization of the NPs and their release in suspension. However, our model suggests that the cohesion of the SCs is independent of the dose rate, which is inconsistent with a disassembly process driven by the beam induced-degradation of CTAC. Another possible explanation relies on an induced positive charge of the SiN membrane building up under electron irradiation due to the generation of secondary electrons.[21] Charging effects at the interface with the SiN membrane have been repeatedly put forward to explain the anomalous diffusive behavior of metal nano-objects in LCTEM that move on the window by sporadic jumps driven by electrostatic repulsion with a dose-rate-dependent frequency.[12] Thus, we infer that the electron beam renders the membrane less adhesive for NPs, because of a charge inversion of the membrane, which would lead to the detachment of the positively charged NPs when Columbic repulsion overcomes the local cohesion energy of SCs. Our model showing the dependence of the adhesion energy with the dose rate supports this hypothesis. Moreover, no NPs were redeposited on the area after ejection, further supporting an irreversible change of the surface state of the membrane. There are several studies in the literature showing conflicting behavior of nanoparticles under the electron beam during LCTEM, with observations of attraction to the image area and motion away from the image area. Studies reporting beam induced self-assembly used negatively charged ligands for the NPs,[12c, 14b, 22] consistent with an increase of the NPs/membrane interaction during imaging. In our case, the NPs are positively charged, so the electron beam renders the membrane less adhesive for NPs, leading to NPs ejection from the image area.[10c, 23] Another study observed different self-assembly behavior (attraction or repulsion) by mitigating solvent polarity in order to adjust electrostatic interaction.[24] All these observations can be rationalized by considering modified electrostatic interaction under electron beam irradiation.

Conclusions

AuNTs and AgNRs were assembled into bulk SCs by depletion-induced self-assembly, forming 3D and 2D superlattices respectively. The structural reconfiguration of the SCs is evidenced after loading them in confined cells used for in situ TEM observations and we show that this effect is induced by a strong NP-membrane interaction. Although the symmetry of the material

is preserved, the affinity of the NPs for the membrane induces the delamination of the SCs into superlattices of lower dimensionality. Moreover, extended beam irradiation leads to disassembly of the lattices, which is well described by a model accounting for the desorption kinetics. This kinetic analysis suggests that the membrane becomes less adhesive upon electron irradiation, leading to NP ejection from the lattices. This work shows that LCTEM can be used to study entropy-driven self-assembly processes, even if caution should be taken to compare with bulk experiments. This works also shed lights on the reconfigurability of SCs obtained by depletion-induced self-assembly, which can rearrange under confinement. This is relevant for applications of these materials in confined geometries or in interaction with charged interfaces.

Experimental section

Materials. Gold chloride trihydrate ($HAuCl_4 \cdot 3H_2O$ ≥99.9%), silver nitrate ($AgNO_3$ >99%), hydrochloric acid (HCl 37%), sodium borohydride ($NaBH_4$ ≥96%), trisodium citrate dihydrate (99%), L-ascorbic acid (AA ≥99%), sodium iodide (NaI 99.9%), cetyltrimethylammonium bromide (CTAB ≥99%), CTAC (25 wt % in H_2O), and benzyldimethylhexadecylammonium chloride (BDAC 99%) were purchased from Merck and used without further purification. All solutions were prepared in water 18.2 MΩ.

Characterization of the NPs. UV/Vis/NIR absorption spectra were collected using a Cary 5000 UV-Vis-NIR. All experiments were carried out at room temperature, using disposable polystyrene cuvettes with optical paths of 1 cm. TEM was performed at IMAGIF (I2BC CNRS, Gif s/Yvette, France) using a JEOL JEM-1400 microscope operating at 120 kV with a filament current of about 55 µA.

Concentration measurement. 10 µL of AuBPs were diluted in 2000 µL of water and the absorbance at 400 nm was recorded with a UV-visible spectrometer in order to estimate the Au(0) concentration, [Au] = 37.3 mM.[25]

Triangles synthesis and purification. The triangles synthesis was performed following the method described by Scarabelli et. al.[15a]

1) **AuNTs synthesis.** Seeds. In a 20 mL vial, 50 µL of $HAuCl_4 \cdot 3H_2O$ (25 mM) were added to 4.7 mL of CTAC (100 mM). Under fast stirring, 300 µL of $NaBH_4$ were added and the reaction medium was left to rest at room temperature for 2 hours.

   AuNTs growth: 2 solutions were prepared freshly and at the same time:

- Solution A: 8 mL of water + 1.6 mL of CTAC (100 mM) + 80 µL of $HAuCl_4 \cdot 3H_2O$ (25mM) + 15 µL of NaI (10 mM) + 40 µL of ascorbic acid (100 mM).

- Solution B: 20 mL of water + 20 mL of CTAC (100 mM) + 1000 µL of $HAuCl_4 \cdot 3H_2O$ (25mM) + 300 µL of NaI (10 mM) + 400 µL of ascorbic acid (100 mM).

As fast as possible and under fast stirring, 100 µL of seeds was added in A, and 3.2 mL of this mixture was added in B. The reaction medium was left to stir gently for 2 hours at room temperature. The particles were then centrifuged and washed with CTAC 10 mM.

2) Purification. The AuNTs were added in a solution of 5 mL of CTAC, with a final concentration of CTAC of 130 mM. The solution was left to rest overnight, the precipitate and the supernatant were carefully separated and analyzed by UV-visible-NIR spectroscopy. The supernatant was discarded; the precipitate was washed and stored in CTAC 10 mM.

Rods synthesis and purification. The AgNRs synthesis consists in overgrowing silver on gold bipyramids (BPs).[15b]

1) Preparation of the gold bipyramids. Seeds. In a 50 mL bottle, 2.65 mL of CTAC (25 wt % in H_2O) and 400 µL of $HAuCl_4$ 25 mM were mixed to 33 mL of water and heated at 30°C for 10 minutes. 4 mL of sodium citrate 50 mM were added and the heating was continued for 30 minutes. Under fast stirring, 1 mL of freshly prepared $NaBH_4$ 25 mM was added, the bottle was closed and put in the oven at 40°C for 5 days. **Bipyramids synthesis.** 500 µL of $AgNO_3$ (100 mM), 10 mL of $HAuCl_4$ (25 mM), and 10 mL of HCl (1 M) were added in 500 mL of CTAB (100 mM). Then, 4 mL of AA (100 mM) was added, followed by 7.5 mL of seeds (15 mL for smaller BPs). After 4 h at 30 °C, the bipyramids were centrifuged twice and purified by depletion during one night at 30 °C in BDAC (350 mM).[26] The supernatant was removed, and the precipitate was redispersed in water and washed twice with 10 mM CTAC. The AuBPs were finally redispersed in 1 mL of 10 mM CTAC. For small BPs, the purification is not possible, the particles were only centrifuged and washed with CTAC 10 mM.

2) Silver overgrowth. 134 µL of BPs were dispersed in a solution of 17.42 mL of water and 2 mL of CTAC 100 mM. The reaction medium was heated to 70°C for 5 minutes and 250 µL of $AgNO_3$ (100 mM, 5 eq) were added, followed by 200 µL of ascorbic acid (500 mM), and heated for 2 hours at 70°C. The particles were centrifuged at an appropriate speed and washed with CTAC 1 mM.

SAXS experiments. The colloidal crystals structures were probed by SAXS at the SWING beamline of the SOLEIL synchrotron (Saint-Aubin, France), using a beam energy of 16 keV and a sample-to-detector distance of 6.481 m. Data treatment (angular averaging and normalization) was done using the Foxtrot software developed at the beamline.

LCTEM. Liquid STEM imaging were simultaneously performed in bright field and dark field modes using an aberration corrected JEOL ARM 200F microscope operating at 200 kV and a liquid-cell TEM holder (Poseidon select, Protochips inc.). A solution of SCs (i.e. colloidal solution with 115 mM of CTAC for the AuNTs and 40 mM CTAC for the AgNRs) was encapsulated in the liquid-cell by using conventional loading process.[27] The Au spacers of the liquid-cells were 150 nm or 500 nm thick. STEM imaging was performed with a probe current of 140 pA measured with a Faraday cup. The electron dose rate of each experiments was automatically calculated in electron.s^{-1}.$Å^2$ by the Axon software (Protochips inc.) by dividing the probe current by the irradiated area (i.e. the image area in STEM mode). We used the magnification to tune the dose rate. Image analysis was performed by image segmentation, using the built-in functions of Matlab software.

Acknowledgement

The CNRS is acknowledged for funding and support. This work had benefited from an Investissements d'Avenir grant from Labex PALM (ANR-10-LABX-0039-PALM) and the ANR Project ARTEMIA. The present work had also benefited from the electronic microscopy facility of Imagerie-Gif, (http://www.i2bc. parissaclay.fr), member of IBiSA (http://www.ibisa.net), supported by "France-BioImaging" (ANR10-INBS-04-01), and the Labex "Saclay Plant Science" (ANR- 11-IDEX-0003-02). The authors acknowledge SOLEIL for the provision of synchrotron radiation facilities (experiment 20210815) and Thomas Bizien for help using the SWING beamline. The authors acknowledge the French national project METSA for supporting the microscope platform of MPQ laboratory.

Supporting Information Available

The Supporting Information is available free of charge at:

Characterization of the NPs, additional SEM images, LCTEM image sequence of the disassembly process are available on-line.

References

[1] a) V. Myroshnychenko, J. Rodriguez-Fernandez, I. Pastoriza-Santos, A. M. Funston, C. Novo, P. Mulvaney, L. M. Liz-Marzan, F. J. Garcia de Abajo, *Chem. Soc. Rev.* **2008**, 37, 1792; b) J. Langer, D. Jimenez de Aberasturi, J. Aizpurua, R. A. Alvarez-Puebla, B. Auguie, J. J. Baumberg, G. C. Bazan, S. E. J. Bell, A. Boisen, A. G. Brolo, J. Choo, D. Cialla-May, V. Deckert, L. Fabris, K. Faulds, F. J. Garcia de Abajo, R. Goodacre, D. Graham, A. J. Haes, C. L. Haynes, C. Huck, T. Itoh, M. Kall, J. Kneipp, N. A. Kotov, H. Kuang, E. C. Le Ru, H. K. Lee, J. F. Li, X. Y. Ling, S. A. Maier, T. Mayerhofer, M. Moskovits, K. Murakoshi, J. M. Nam, S. Nie, Y. Ozaki, I. Pastoriza-Santos, J. Perez-Juste, J. Popp, A. Pucci, S. Reich, B. Ren, G. C. Schatz, T. Shegai, S. Schlucker, L. L. Tay, K. G. Thomas, Z. Q. Tian, R. P. Van Duyne, T. Vo-Dinh, Y. Wang, K. A. Willets, C. Xu, H. Xu, Y. Xu, Y. S. Yamamoto, B. Zhao, L. M. Liz-Marzan, *ACS Nano* **2020**, 14, 28; c) R. Alvarez-Puebla, L. M. Liz-Marzán, F. J. García de Abajo, *J. Phys. Chem. Lett.* **2010**, 1, 2428.

[2] M. Grzelczak, L. M. Liz-Marzan, R. Klajn, *Chem. Soc. Rev.* **2019**, 48, 1342.

[3] K. J. M. Bishop, C. E. Wilmer, S. Soh, B. A. Grzybowski, *Small* **2009**, 5, 1600.

[4] a) H. N. W. Lekkerkerker, R. Tuinier, in *Colloids and the Depletion Interaction*, DOI: 10.1007/978-94-007-1223-2_2, Springer Netherlands, Dordrecht **2011**, p. 57; b) S. Asakura, F. Oosawa, *J. Chem. Phys.* **1954**, 22, 1255; c) S. Asakura, F. Oosawa, *J. Pol. Sci.* **1958**, 33, 183; d) D. Baranov, A. Fiore, M. van Huis, C. Giannini, A. Falqui, U. Lafont, H. Zandbergen, M. Zanella, R. Cingolani, L. Manna, *Nano Lett.* **2010**, 10, 743; e) M. H. Huang, S. Thoka, *Nano Today* **2015**, 10, 81.

[5] D. Frenkel, *Nat. Mater.* **2015**, 14, 9.

[6] a) N. R. Jana, *Chem. Commun.* **2003**, 1950; b) K. Park, H. Koerner, R. A. Vaia, *Nano Lett.* **2010**, 10, 1433; c) L. Scarabelli, M. Coronado-Puchau, J. J. Giner-Casares, J. Langer, L. M. Liz-Marzán, *ACS Nano* **2014**, 8, 5833.

[7] a) D. García-Lojo, E. Modin, S. Gómez-Graña, M. Impéror-Clerc, A. Chuvilin, I. Pastoriza-Santos, J. Pérez-Juste, D. Constantin, C. Hamon, *Adv. Funct. Mater.* **2021**, 31, 2101869; b) J. Lyu, W. Chaabani, E. Modin, A. Chuvilin, T. Bizien, F. Smallenburg, M. Imperor-Clerc, D. Constantin, C. Hamon, *Adv. Mater.* **2022**, 34, e2200883; c) J. Gong, R. S. Newman, M. Engel, M. Zhao, F. Bian, S. C. Glotzer, Z. Tang, *Nat. Commun.* **2017**, 8, 14038; d) T. Ming, X. Kou, H. Chen, T. Wang, H.-L. Tam, K.-W. Cheah, J.-Y. Chen, J. Wang, *Angew. Chem. Int. Ed.* **2008**, 120, 9831; e) J. Kim, X. Song, F. Ji, B. Luo, N. F. Ice, Q. Liu, Q. Zhang, Q. Chen, *Nano Lett.* **2017**, 17, 3270; f) J.

Marcone, W. Chaabani, C. Goldmann, M. Imperor-Clerc, D. Constantin, C. Hamon, *Nano Lett.* **2023**, 23,1337.

[8] a) K. L. Young, M. R. Jones, J. Zhang, R. J. Macfarlane, R. Esquivel-Sirvent, R. J. Nap, J. Wu, G. C. Schatz, B. Lee, C. A. Mirkin, *Proc. Natl. Acad. Sci.* **2012**, 109, 2240; b) C.-W. Yang, C.-Y. Chiu, M. H. Huang, *Chem. Mater.* **2014**, 26, 4882; c) P.-W. Yang, S. Thoka, P.-C. Lin, C.-J. Su, H.-S. Sheu, M. H. Huang, U. S. Jeng, *Langmuir* **2017**, 33, 3253; d) K. L. Young, M. L. Personick, M. Engel, P. F. Damasceno, S. N. Barnaby, R. Bleher, T. Li, S. C. Glotzer, B. Lee, C. A. Mirkin, *Angew. Chem. Int. Ed.* **2013**, 52, 13980.

[9] a) N. de Jonge, F. M. Ross, *Nat. Nanotechnol.* **2011**, 6, 695; b) F. M. Ross, *Science* **2015**, 350, aaa9886; c) A. Khelfa, J. Nelayah, H. Amara, G. Wang, C. Ricolleau, D. Alloyeau, *Adv. Mater.* **2021**, 33, 2102514.

[10] a) Z. Ou, Z. Wang, B. Luo, E. Luijten, Q. Chen, *Nat. Mater.* **2020**, 19, 450; b) X. Ye, M. R. Jones, L. B. Frechette, Q. Chen, A. S. Powers, P. Ercius, G. Dunn, G. M. Rotskoff, S. C. Nguyen, V. P. Adiga, A. Zettl, E. Rabani, P. L. Geissler, A. P. Alivisatos, *Science* **2016**, 354, 874; c) Z. Ou, C. Liu, L. Yao, Q. Chen, *Acc. Mater. Res.* **2020**, 1, 41; d) S. Pu, C. Gong, A. W. Robertson, *Royal Soc. Open Sci.* **2020**, 7, 191204; e) S. Zhou, J. Li, J. Lu, H. Liu, J.-Y. Kim, A. Kim, L. Yao, C. Liu, C. Qian, Z. D. Hood, X. Lin, W. Chen, T. E. Gage, I. Arslan, A. Travesset, K. Sun, N. A. Kotov, Q. Chen, *Nature* **2022**, 612, 259.

[11] a) A. Bo, Y. Liu, B. Kuttich, T. Kraus, A. Widmer-Cooper, N. de Jonge, *Adv. Mater.* **2022**, 34, 2109093; b) Q. Chen, J. M. Yuk, M. R. Hauwiller, J. Park, K. S. Dae, J. S. Kim, A. P. Alivisatos, *MRS Bull.* **2020**, 45, 713.

[12] a) M. Piffoux, N. Ahmad, J. Nelayah, C. Wilhelm, A. Silva, F. Gazeau, D. Alloyeau, *Nanoscale* **2018**, 10, 1234; b) A. Verch, M. Pfaff, N. de Jonge, *Langmuir* **2015**, 31, 6956; c) T. J. Woehl, T. Prozorov, *J. Phys. Chem. C* **2015**, 119, 21261; d) V. Jamali, C. Hargus, A. Ben-Moshe, A. Aghazadeh, H. D. Ha, K. K. Mandadapu, A. P. Alivisatos, *Proc. Natl. Acad. Sci.* **2021**, 118, e2017616118; e) E. Bakalis, L. R. Parent, M. Vratsanos, C. Park, N. C. Gianneschi, F. Zerbetto, *J. Phys. Chem. C* **2020**, 124, 14881.

[13] a) T. J. Woehl, P. Abellan, *J. Microsc.* **2017**, 265, 135; b) N. M. Schneider, M. M. Norton, B. J. Mendel, J. M. Grogan, F. M. Ross, H. H. Bau, *J. Phys. Chem. C* **2014**, 118, 22373; c) T. U. Dissanayake, M. Wang, T. J. Woehl, *ACS Appl. Mater.* **2021**, 13, 37553.

[14] a) K. Aliyah, J. Lyu, C. Goldmann, T. Bizien, C. Hamon, D. Alloyeau, D. Constantin, *J. Phys. Chem. Lett.* **2020**, 11, 2830; b) J. Kim, M. R. Jones, Z. Ou, Q. Chen, *ACS Nano* **2016**, 10, 9801; c) A. Khelfa, J. Meng, C. Byun, G. Wang, J. Nelayah, C. Ricolleau, H. Amara, H. Guesmi, D. Alloyeau, *Nanoscale* **2020**, 12, 22658.

[15] a) L. Scarabelli, L. M. Liz-Marzan, *ACS Nano* **2021**, 15, 18600; b) X. Zhuo, X. Zhu, Q. Li, Z. Yang, J. Wang, *ACS Nano* **2015**, 9, 7523.

[16] W. Han, Z. Lin, *Angew. Chem. Int. Ed.* **2012**, 51, 1534.

[17] S. Gomez-Grana, F. Hubert, F. Testard, A. Guerrero-Martinez, I. Grillo, L. M. Liz-Marzan, O. Spalla, *Langmuir* **2012**, 28, 1453.

[18] a) K. Liu, Z. Nie, N. Zhao, W. Li, M. Rubinstein, E. Kumacheva, *Science* **2010**, 329, 197; b) J. Lyu, D. Alloyeau, C. Hamon, D. Constantin, *J. Mater. Chem. C* **2021**, 9, 1730.

[19] a) M. Matusiak, S. Kadlubowski, J. M. Rosiak, *Radiat. Phys. Chem.* **2020**, 169, 108099; b) G. Ungar, *J. Mater. Sci.* **1981**, 16, 2635; c) I. A. Shkrob, A. D. Trifunac, *Radiat. Phys. Chem.* **1995**, 46, 83; d) Z. Guo, H. Hong, Y. Zheng, Z. Wang, Z. Ding, Q. Fu, Z. Liu, *Angew. Chem. Int. Ed.* **2022**, 61, e202205014.

[20] M. Wang, C. Park, T. J. Woehl, *Chem. Mater.* **2018**, 30, 7727.

[21] a) J. Cazaux, *Ultramicroscopy* **1995**, 60, 411; b) Y. Wang, D. Rastogi, K. Malek, J. Sun, A. Asa-Awuku, T. J. Woehl, *J. Phys. Chem. A* **2023**, 127, 2545.

[22] J. Kim, Z. Ou, M. R. Jones, X. Song, Q. Chen, *Nat. Commun.* **2017**, 8, 761.

[23] B. H. Kim, J. Yang, D. Lee, B. K. Choi, T. Hyeon, J. Park, *Adv. Mater.* **2018**, 30, 1703316.

[24] Y. Zhong, V. R. Allen, J. Chen, Y. Wang, X. Ye, *J. Am. Chem. Soc.* **2022**, 144, 14915.

[25] a) T. Hendel, M. Wuithschick, F. Kettemann, A. Birnbaum, K. Rademann, J. Polte, *Anal. Chem.* **2014**, 86, 11115; b) L. Scarabelli, A. Sánchez-Iglesias, J. Pérez-Juste, L. M. Liz-Marzán, *J. Phys. Chem. Lett.* **2015**, 6, 4270.

[26] J. H. Lee, K. J. Gibson, G. Chen, Y. Weizmann, *Nat. Commun.* **2015**, 6, 7571.

[27] A. Khelfa, J. Nelayah, G. Wang, C. Ricolleau, D. Alloyeau, *J. Vis. Exp.* **2021**, DOI: 10.3791/62225.